

RadImageGAN – A Multi-modal Dataset-Scale Generative AI for Medical Imaging

¹Zelong Liu, ¹Alexander Zhou, ¹Arnold Yang, ¹Alara Yilmaz, ¹Maxwell Yoo, ¹Mikey Sullivan, ¹Catherine Zhang, ¹James Grant, ²Daiqing Li, ^{1,5}Zahi A. Fayad, ^{2,5}Sean Huver, ^{3,4,5}Timothy Deyer, ^{1,5}Xueyan Mei

¹BioMedical Engineering and Imaging Institute, Icahn School of Medicine at Mount Sinai, New York, NY

²NVIDIA, Santa Clara, CA

³East River Medical Imaging, New York, NY

⁴Department of Radiology, Cornell Medicine, New York, NY

⁵These authors jointly supervised this work.

Corresponding authors: Zahi Fayad, email: zahi.fayad@mssm.edu; Sean Huver, email: shuver@nvidia.com; Timothy Deyer, email: tdeyer@eastriverimaging.com; Xueyan Mei, email: xueyan.mei@icahn.mssm.edu.

ABSTRACT

Deep learning in medical imaging often requires large-scale, high-quality data or initiation with suitably pre-trained weights. However, medical datasets are limited by data availability, domain-specific knowledge, and privacy concerns, and the creation of large and diverse radiologic databases like RadImageNet is highly resource-intensive. To address these limitations, we introduce RadImageGAN, the first multi-modal radiologic data generator, which was developed by training StyleGAN-XL on the real RadImageNet dataset of 102,774 patients. RadImageGAN can generate high-resolution synthetic medical imaging datasets across 12 anatomical regions and 130 pathological classes in 3 modalities. Furthermore, we demonstrate that RadImageGAN generators can be utilized with BigDatasetGAN to generate multi-class pixel-wise annotated paired synthetic images and masks for diverse downstream segmentation tasks with minimal manual annotation.

We showed that using synthetic auto-labeled data from RadImageGAN can significantly improve performance on four diverse downstream segmentation datasets by augmenting real training data and/or developing pre-trained weights for fine-tuning. This shows that RadImageGAN combined with BigDatasetGAN can improve model performance and address data scarcity while reducing the resources needed for annotations for segmentation tasks.

KEY POINTS

1. The RadImageGAN generator can produce high-quality multi-class/modality synthetic images across 130 pathologies and 12 anatomies in CT, MRI, and endoscopy imaging modalities
2. BigDatasetGAN can be used with RadImageGAN to generate paired masks for fully labeled multi-class synthetic images with a weakly supervised approach requiring minimal manual annotation
3. Using synthetic labeled imaging data to develop pre-trained weights for transfer learning (“synthetic pretraining”) and/or augmenting real medical imaging datasets in training (“synthetic augmentation”) can significantly boost performance on downstream segmentation applications, particularly when the downstream datasets are small

INTRODUCTION

Medical imaging has revolutionized the field of healthcare over the past century by providing accurate and non-invasive diagnostic tools. Within the last ten years, machine learning has undergone a parallel revolution in healthcare, providing diagnostic, predictive, and treatment models for medical imaging leading to increased diagnostic accuracy, improved treatment effectiveness, and cost efficiencies (1,2). To reach these performance standards, models require large representative volumes of high-quality medical imaging data (1,3). However, the data collection and manual annotation of medical images for training these models is a time-consuming and resource-intensive task requiring expert medical domain knowledge, which limits the size and diversity of available datasets for machine learning applications (4). Furthermore, the publication and sharing of medical datasets are limited by significant privacy and regulatory concerns (5–9), resulting in datasets that are limited in size and scope, data siloing within health systems, and unbalanced representation of general populations or other rarer conditions. Addressing these issues will unlock the full potential of machine learning in developing novel medical applications and delivering enhanced healthcare.

Recently, RadImageNet was curated as a large-scale radiological image database that contains 1.35 million images in 3 modalities (CT, MRI, and US) labeled with 165 pathologic classes on 11 anatomic regions, making it a valuable resource for training deep learning models (10). However, the creation of such a database was resource-intensive, requiring significant amounts of time and expertise to collect and annotate images.

Traditional methods to circumvent these data limitations include transfer learning from larger and/or out-of-domain datasets and basic data augmentation on existing image data (e.g., geometric transformations, random erasing, image mixing, kernel filtering). However, these methods do not solve the fundamental issue of data availability. More recently, generative machine learning approaches are being studied to enable the creation of synthetic medical imaging datasets with similar aggregate statistical characteristics to real source datasets for various applications in medical imaging. A promising paradigm that has emerged is the use of generative adversarial networks (GANs) (11) to create synthetic medical images for the training of machine learning models (12–17).

Gao et al. developed SyntheX, a framework for developing generalizable AI algorithms from annotated computed tomography (CT), to generate synthetic X-ray images for model training and achieved comparable or better performance than CycleGAN (18) and other models trained directly on real data in three downstream clinical tasks (hip imaging segmentation, surgical robotic tool detection, and COVID-19 lesion segmentation) (19). Guo et al. proposed MedGAN, a GAN architecture using Wasserstein loss as a convergence metric, which was used to generate medical images for few-shot learning models on various disease classification and lesion localization datasets (15). Gheorghiu et al. used a GauGAN model (20) to generate synthetic short-axis cardiac Cine magnetic resonance imaging (MRI) scans for convolutional neural network (CNN) pretraining, which significantly improved cardiac function quantification (21). Other work demonstrated the use of GANs for synthetic data augmentation in liver lesion classification (14) and generation of indistinguishable high-resolution chest radiograph synthesis (22), aggregated GANs for brain tumor image generation (23), and pix2pix-based GAN for lung cancer computed tomography (CT) images (24).

However, these approaches are limited, as these generative architectures are typically restricted to synthesizing imaging data in a specific modality, anatomy, and/or pathology. Furthermore, the generated imaging data may lack semantic segmentation, which could provide further downstream utility.

In this study, we propose training StyleGAN-XL, a new state-of-the-art GAN model that scales StyleGAN for multi-class large unstructured datasets (25), on RadImageNet to generate synthetic radiological images that fall within the diagnostic classes of RadImageNet. With this approach, we aim to develop a multi-class radiologic data generator, which we term “**RadImageGAN**”, that can generate synthetic labeled multi-class medical images. In this study, we specifically develop 2 generators: “**RadImageGAN-CT/MR**”, which generates CT and MR images with 124 pathological classes created from the real data of 102,774 patients, and “**RadImageGAN-Gastro**”, which generates gastrointestinal colonoscopy video images with 6 pathological classes, for a total of 130 classes.

To further enhance the utility of RadImageGAN, we then aim to apply BigDatasetGAN (26) to RadImageGAN to develop a multi-class, pixel-wise label generator of RadImageGAN synthetic images, “**RadImageGAN-Labeled**”. BigDatasetGAN is a GAN-based approach that can generate pixel-wise labeled synthetic images with a small set of manually labeled GAN-generated images. Applying BigDatasetGAN to RadImageGAN allows us to generate multi-class synthetic and fully annotated images with minimal manual labeling effort, which can then be used to create large-scale datasets for training segmentation models and augment downstream segmentation datasets.

The approach and utility of this new paradigm is illustrated in **Figure 1**. In this study, we demonstrate the ability of RadImageGAN to generate high-quality multi-class synthetic CT and MR imaging and its ability to boost performance in medical imaging segmentation tasks in diverse data availability conditions (low, moderate, and full real data availability) when combined with BigDatasetGAN. Improved performance comes from using RadImageGAN for: 1) synthetic data augmentation of real datasets for model training (“**synthetic augmentation**”) and 2) development of pre-trained weights from synthetic data for downstream transfer learning (“**synthetic pretraining**”). We find that our RadImageGAN-generated synthetic labeled images and pre-trained weights can significantly boost segmentation performance compared to models solely trained on real data under most data availability conditions.

RESULTS

StyleGAN-XL training for RadImageGAN

StyleGAN-XL models can generate high-resolution synthetic images by learning from large and diverse unstructured datasets. This new state-of-the-art approach enables our vision to generate large numbers of high-resolution synthetic medical images across pathologies, modalities, and anatomies. Using 8 NVIDIA DGX-A100 GPUs with 640GB VRAM, the RadImageGAN-CT/MR model was trained on the 0.88 million CT/MR images and 124 corresponding unique pathological labels from the RadImageNet database. **Table S2** summarizes the training progress of RadImageGAN-CT/MR from low resolution (16x16 px) to high resolution (512x512 px) image output over 4,563 A100 computational hours. The Fréchet inception distance (FID) score

was 6.40, 7.75, 7.60, 8.85, 9.23, and 9.37 at the output resolution stages of 16x16, 32x32, 64x64, 128x128, 256x256, and 512x512 px, respectively.

The RadImageGAN-Gastro model was developed on a subset of the HyperKvasir gastrointestinal dataset consisting of 6 pathological labels and 5,713 images from colonoscopy procedures (27). **Table S3** summarizes the training progress of RadImageGAN-Gastro on 8 NVIDIA DGX-V100 GPUs with 256GB VRAM over 3,088 computational hours. The FID score was 8.08, 9.12, 11.36, 8.74, 5.50, and 5.05 at the output resolution stages of 16x16, 32x32, 64x64, 128x128, 256x256, and 512x512 px, respectively.

Figures 2 and 3, and **Table S1** provide illustrative examples and summarize the modalities, views, anatomies, and labels that RadImageGAN is able to generate. Generator training time and performance are summarized in **Tables S2 and S3**.

Training and performance of RadImageGAN-Labeled on downstream applications

To assess the utility of RadImageGAN-CT/MR and RadImageGAN-Gastro in diverse downstream medical applications, the following four public segmentation datasets and tasks were selected for their diversity in anatomy, modality, and pathology: BTCV-Abdomen (abdominal CT) (28), CHAOS-MRI (abdominal MRI) (29), Labeled Lumbar Spine MRI (spinal MRI) (30), and CVC-ClinicDB (gastrointestinal endoscopy images) (31). For BTCV-Abdomen, the normal abdomen CT class from RadImageGAN-CT/MR was used for synthetic generation, and BigDatasetGAN was then used to develop an automatic mask generator for liver and kidney segmentation. For CHAOS-MRI, the normal abdomen MRI class from RadImageGAN-CT/MR was used for synthetic generation, and BigDatasetGAN was then used to develop an automatic mask generator for liver and kidney segmentation. For Labeled Lumbar Spine MRI, the spinal canal stenosis MRI class from RadImageGAN-CT/MR was used for synthetic generation, and BigDatasetGAN was then used to develop an automatic mask generator for intervertebral disc (IVD), posterior element (PE), and thecal sac (TS) segmentation. For CVC-ClinicDB, synthetic images of the polyp colonoscopy imaging class from RadImageGAN-Gastro were used for synthetic generation, and BigDatasetGAN was then used to develop an automatic mask generator for polyp segmentation. Downstream tasks are summarized in **Table S8**.

For each downstream task, the efficacy of the synthetic images for data augmentation in model training (“**synthetic augmentation**”) was assessed by training nnU-Net models (32) under 10 data conditions for each of the 4 datasets with varying proportions of real and synthetic imaging data. The data conditions are summarized in **Table 1**. The BTCV-Abdomen and CHAOS-MRI datasets collected data by patient scans, so those minimal and low real data conditions used real imaging data from 1 and 2 full patient scans, respectively. The Labeled Lumbar Spine MRI and CVC-ClinicDB datasets collected data at a slice level, so those minimal and low real data conditions used 1% and 10% of total available real slice images, respectively. Synthetic augmentation was then used to add synthetic images such that the augmented training dataset was approximately the same size as the full real training dataset, which we call “synthetic gap augmentation.” For full real data conditions, we used the full real training datasets and augmented them with different amounts of synthetic images (10%, 50%, and 100% of the full real training dataset size).

The efficacy of these synthetic images for transfer learning (“**synthetic pretraining**”) was also assessed by pretraining a nnU-Net model for each of the 4 datasets on a corresponding synthetic dataset similarly sized to each of the real training datasets and subsequently fine-tuning each of the 4 pre-trained models under the same 10 data conditions. This assessed the effects of fine-tuning synthetically pretrained models with both purely real and augmented datasets.

Performance was quantified by the average Dice score of resulting segmentation on test datasets in all experiments. A summary of the relative effects of the two synthetic methods in all experiments is shown in **Figure 4**.

BTCV-Abdomen

The BTCV-Abdomen dataset consists of 30 abdominal CT patient scans. For each fold of the five-fold cross-validation, the minimal/low/moderate/full real training data condition was defined as 1/2/11(50%)/22(100%) patient abdominal scans; 2 scans were used for validation, and 6 scans were used for testing. Results are summarized in **Table 2a**, and corresponding statistics in **Tables S4a** and **S4b**.

For the BTCV-Abdomen dataset, training nnU-Net models in minimal real data conditions (1 scan) achieved an average Dice score of 0.582/0.482 on liver/kidney segmentation. Synthetic gap augmentation in training boosted performance to 0.678/0.645 on liver/kidney segmentation ($p < 0.001 / < 0.001$). Using a pre-trained model and fine-tuning on minimal real data boosted performance to 0.636/0.590 ($p < 0.001 / p < 0.001$), while using a pre-trained model and fine-tuning on minimal real data with synthetic gap augmentation yielded similar results (0.677/0.654; $p < 0.001 / p < 0.001$) to solely training on minimal real data with synthetic gap augmentation without synthetic pretraining.

Training in low real data conditions (2 scans) achieved an average Dice score of 0.648/0.582 on liver/kidney segmentation. Synthetic gap augmentation in training boosted performance to 0.713/0.675 on liver/kidney segmentation ($p = 0.971 / p < 0.001$). Using a pre-trained model and fine-tuning on low real data boosted performance to 0.698/0.677 ($p < 0.001 / p < 0.001$), while using a pre-trained model and fine-tuning on low real data with synthetic gap augmentation yielded similar results (0.702/0.673; $p = 0.468 / p < 0.001$) to solely training on low real data with synthetic gap augmentation without synthetic pretraining.

Training on moderate real data conditions (11 scans) achieved an average Dice score of 0.823/0.813 on liver/kidney segmentation. Synthetic gap augmentation mildly boosted performance to 0.829/0.825 ($p < 0.001 / p < 0.001$). Using a pre-trained model and fine-tuning on moderate real data boosted performance to 0.846/0.833 ($p < 0.001 / p < 0.001$), while using a pre-trained model and fine-tuning on moderate data with synthetic gap augmentation yielded similar results (0.837/0.823; $p < 0.001 / p < 0.001$) to solely training on moderate data with synthetic gap augmentation without synthetic pretraining.

Training on full real data conditions (all 22 scans) achieved an average Dice score of 0.833/0.832 on liver/kidney segmentation. Augmenting with 10%, 50%, and 100% synthetic data yielded similar performances of 0.834/0.856, 0.845/0.854, and 0.841/0.847, respectively ($p < 0.001 / p = 0.710$, $p < 0.001 / p = 0.061$, $p < 0.001 / p < 0.01$). Using a pre-trained model and fine-tuning on full real data boosted performance to 0.852/0.863 ($p < 0.001 / p < 0.001$), while using a

pre-trained model and fine-tuning on full real data with 10%, 50%, and 100% synthetic data augmentation yielded similar results of 0.847/0.865, 0.841/0.849, and 0.847/0.850, respectively ($p=0.104/p=0.133$, $p<0.001/p=0.379$, $p<0.001/p<0.01$).

CHAOS-MRI

The CHAOS-MRI dataset consists of 20 T2 abdominal MRI patient scans. For each fold of the five-fold cross-validation, the minimal/low/moderate/full real data condition was defined as 1/2/7(50%)/14(100%) patient abdominal scans; 2 scans were used for validation, and 4 scans were used for testing. Results are summarized in **Table 2b**, and corresponding statistics in **Tables S5a** and **S5b**.

For the CHAOS-MRI dataset, training nnU-Net models in minimal real data conditions (1 scan) achieved an average Dice score of 0.446/0.394 on liver/kidney segmentation. Synthetic gap augmentation in training boosted performance to 0.549/0.563 on liver/kidney segmentation ($p<0.001/p<0.001$). Using a pre-trained model and fine-tuning on minimal real data boosted performance to 0.472/0.476 ($p=0.325/p<0.001$), while using a pre-trained model and fine-tuning on minimal real data with synthetic gap augmentation yielded similar results (0.571/0.538; $p<0.001/p<0.001$) to solely training on minimal real data with synthetic gap augmentation without synthetic pretraining.

Training in low real data conditions (2 scans) achieved an average Dice score of 0.578/0.579 on liver/kidney segmentation. Synthetic gap augmentation boosted performance to 0.611/0.676 on liver/kidney segmentation ($p=0.560/p<0.001$). Using a pre-trained model and fine-tuning on low real data boosted performance to 0.584/0.613 ($p=0.118/p<0.01$), while using a pre-trained model and fine-tuning on low real data with synthetic gap augmentation yielded similar results (0.626/0.659; $p=0.987/p<0.001$) to solely training on low real data with synthetic gap augmentation without synthetic pretraining.

Training on moderate real data conditions (7 scans) achieved an average Dice score of 0.692/0.818 on liver/kidney segmentation. Synthetic gap augmentation yielded similar performance of 0.702/0.792 ($p=0.640/p<0.01$). Using a pre-trained model and fine-tuning on moderate real data led to decreased performance at 0.609/0.678 ($p<0.001/p<0.001$), while using a pre-trained model and fine-tuning on moderate data with synthetic gap augmentation also led to decreased performance (0.618/0.642; $p<0.001/p<0.001$).

Training on full real data conditions (all 14 scans) achieved an average Dice score of 0.750/0.845 on liver/kidney segmentation. Augmenting with 10%, 50%, and 100% synthetic data yielded similar performances of 0.766/0.849, 0.763/0.862, and 0.757/0.857, respectively ($p<0.05/p=0.315$, $p=0.737/p=0.726$, $p<0.05/p=0.368$). Using a pre-trained model and fine-tuning on full real data yielded a similar performance of 0.727/0.846 ($p<0.001/p=0.309$) while using a pre-trained model and fine-tuning on full real data with 10%, 50%, and 100% of synthetic data augmentation yielded decreased performance of 0.667/0.769, 0.644/0.711, and 0.682/0.753, respectively ($p<0.001/p<0.001$, $p<0.001/p<0.001$, $p<0.001/p<0.001$).

Labeled Lumbar Spine MRI

The Labeled Lumbar Spine MRI dataset consists of 1,545 T2 MRI images. For each fold of the 5-fold cross-validation, the minimal/low/moderate/full real data condition was defined as

6/30/555/1113 of the MRI images; 123 images were used for validation, and 309 images were used for testing. Results are summarized in **Table 2c**, and corresponding statistics in **Tables S6a**, **S6b**, and **S6c**.

For the Labeled Lumbar Spine MRI dataset, training nnU-Net models in minimal real data conditions achieved an average Dice score of 0.924/0.772/0.852 on IVD/TS/PE segmentation. Synthetic gap augmentation in training yielded performance of 0.919/0.700/0.779 on IVD/TS/PE segmentation ($p < 0.001/p < 0.001/p < 0.001$). Using a pre-trained model and fine-tuning on minimal real data boosted performance to 0.957/0.831/0.893 ($p < 0.001/p < 0.001/p < 0.001$), while using a pre-trained model and fine-tuning on minimal real data with 99% synthetic data augmentation yielded similar results (0.924/0.715/0.788; $p < 0.001/p < 0.001/p < 0.001$) to solely training on minimal real data with synthetic gap augmentation without pretraining .

Training in low real data conditions achieved an average Dice score of 0.967/0.857/0.907 on IVD/TS/PE segmentation. Synthetic gap augmentation in training yielded performance of 0.941/0.776/0.835 on IVD/TS/PE segmentation ($p < 0.001/p < 0.001/p < 0.001$). Using a pre-trained model and fine-tuning on low real data yielded similar performance as without pretraining (0.970/0.867/0.912, $p < 0.001/p < 0.001/p < 0.001$), while using a pre-trained model and fine-tuning on low real data with synthetic gap augmentation yielded similar results (0.945/0.789/0.843; $p < 0.001/p < 0.001/p < 0.001$) to solely training on low real data with synthetic gap augmentation without pretraining.

Training on moderate real data conditions achieved an average Dice score of 0.974/0.899/0.927 on IVD/TS/PE segmentation. Synthetic gap augmentation in training yielded a similar performance of 0.973/0.893/0.924 ($p < 0.001/p < 0.001/p < 0.001$). Using a pre-trained model and fine-tuning on moderate real data yielded similar performance of 0.975/0.901/0.928 ($p < 0.001/p < 0.001/p < 0.001$), while using a pre-trained model and fine-tuning on moderate data with synthetic gap augmentation yielded similar results (0.973/0.892/0.924; $p < 0.001/p < 0.001/p < 0.001$) to solely training on moderate data with synthetic gap augmentation without pretraining.

Training on full real data conditions achieved an average Dice score of 0.975/0.906/0.929 on IVD/TS/PE segmentation. Augmenting with 10%, 50%, and 100% synthetic data yielded similar performances of 0.975/0.905/0.928, 0.975/0.902/0.927, and 0.974/0.900/0.926, respectively (see **Table S6a-c** for associated p values). Using a pre-trained model and fine-tuning on full real data boosted performance to 0.976/0.907/0.929 ($p < 0.001/p = 0.207/p < 0.05$) while using a pre-trained model and fine-tuning on full real data with 10%, 50%, and 100% of synthetic data augmentation yielded similar results (0.975/0.905/0.929, 0.975/0.902/0.927, 0.974/0.899/0.926) (see **Table S6a-c** for associated p values).

CVC-ClinicDB

The CVC-ClinicDB dataset consists of 612 still images from endoscopic colonoscopy videos with segmented polyps. The minimal/low/moderate/full real data condition was defined as 5(1%)/44(10%)/220(50%)/440(100%) of the MRI images; 49 images were used for validation, and 123 images were used for testing. Results are summarized in **Table 2d**, and corresponding statistics in **Table S7**.

For the CVC-ClinicDB dataset, training nnU-Net models in minimal real data conditions (1% of images) achieved an average Dice score of 0.377 on polyp segmentation. Synthetic gap augmentation in training significantly boosted performance to 0.685 on polyp segmentation ($p < 0.001$). Using a pre-trained model and fine-tuning on minimal real data significantly boosted performance to 0.624 ($p < 0.001$), while using a pre-trained model and fine-tuning on minimal real data with synthetic gap augmentation yielded similar results (0.697; $p < 0.001$) to solely training on minimal real data with synthetic gap augmentation without synthetic pretraining.

Training in low real data conditions (10% of images) achieved an average Dice score of 0.656 on polyp segmentation. Synthetic gap augmentation in training boosted performance to 0.755 on polyp segmentation ($p < 0.001$). Using a pre-trained model and fine-tuning on low real data boosted performance to 0.795 ($p < 0.001$), while using a pre-trained model and fine-tuning on low real data with synthetic gap augmentation yielded similar results (0.762; $p < 0.001$) to training on low real data with synthetic gap augmentation without synthetic pretraining.

Training on moderate real data conditions (50% of images) achieved an average Dice score of 0.788 on polyp segmentation. Synthetic gap augmentation boosted performance to 0.830 ($p < 0.001$). Using a pretrained model and fine-tuning on moderate real data boosted performance to 0.837 ($p < 0.001$), while using a pre-trained model and fine-tuning on moderate data with synthetic gap augmentation yielded similar results (0.837; $p < 0.001$) to training on moderate data with synthetic gap augmentation without synthetic pretraining.

Training on full real data conditions (all 612 images) achieved an average Dice score of 0.798 on polyp segmentation. Augmenting with 10%, 50%, and 100% synthetic data yielded improved performance of 0.819, 0.832, and 0.830, respectively ($p < 0.001$, $p < 0.001$, $p < 0.001$). Using a pre-trained model and fine-tuning on full real data boosted performance to 0.841 ($p < 0.001$), while using a pre-trained model and fine-tuning on full real data with 10%, 50%, and 100% synthetic data augmentation yielded similar results 0.842, 0.845, 0.844, respectively ($p < 0.001$, $p < 0.001$, $p < 0.001$).

DISCUSSION

In medical imaging, the generation of large and robust fully labeled imaging datasets is challenging due to the time and expertise required to manually annotate pixel-wise segmentation masks, as well as the limited public availability of medical imaging due to privacy and regulatory concerns. These data limitations are consistently documented in the literature and pose a significant challenge for training machine learning models for medical imaging (33,34). While pre-trained weights for classification tasks are more readily accessible due to their generic nature, pre-trained weights tailored for segmentation are inherently task-specific, further emphasizing the importance of developing robust labeled datasets to improve segmentation outcomes in medical imaging applications.

GANs have been studied for their potential use to generate synthetic medical images for diverse applications. One specific paradigm is the use of GANs to produce synthetic images for machine learning model training to enhance performance on downstream segmentation tasks. Work by Guo et al. in developing MedGAN (15) and Osuala et al. in developing medigan (35) illustrate the potential for this paradigm to synthetically augment real datasets and boost segmentation performance, particularly in low data availability conditions.

However, while these studies utilized GANs to generate unlabeled synthetic medical images of a single/limited class or modality, our proposed RadImageGAN paradigm extends these capabilities and enables the generation of synthetic images from a plethora of imaging modalities, sequences, and pathologies. In this study, we excluded the ultrasound modality from RadImageNet due to its variations in orientation compared to CT and MRI, which would have negatively affected the development of the RadImageGAN generator. In addition to radiologic imaging, we expanded our scheme to colonoscopy imaging to examine the potential of synthetic imaging for other medical imaging modalities. Because colonoscopy is a domain of medical imaging techniques fundamentally different from radiological imaging, we developed two separate generators, RadImageGAN-CT/MR and RadImageGAN-Gastro. The 2 generators we trained in this study are able to generate medical images from 130 pathological classes, 3 modalities, and 12 anatomical regions. Moreover, with only a modest number of manual annotations per task, BigDatasetGAN further enables the generation of accurate pixel-wise segmentation masks on these synthetic data (RadImageGAN-Labeled). Our proposed deep learning paradigm enables the use of synthetic labeled images for real downstream applications to boost segmentation performance with two methods: 1) first, as a method of synthetic data augmentation (“synthetic augmentation”), and 2) as synthetic source data for developing pre-trained weights for transfer learning (“synthetic pretraining”).

Figure 4 illustrates performance on the diverse downstream segmentation tasks assessed in this study under various data availability conditions and synthetic enhancements. Note that using synthetic augmentation and/or pretraining was able to boost performance on all segmentation tasks in nearly all data availability conditions relative to training on solely real data. There are several data situations in which synthetic enhancement is particularly effective, as well as a few data situations in which synthetic enhancement may lead to poorer performance.

Generally, we find that in minimal/low data condition scenarios, adding synthetic data and/or using synthetic pre-trained weights can boost segmentation performance significantly. Combining both synthetic methods may sometimes yield further improvements in sparse data conditions, but we generally observe that the greatest improvements come from applying a single synthetic method. It is possible that using both methods might cause overfitting in learning synthetic image features during training.

We also find that for tasks in which relatively high performance was already achieved in minimal/low data conditions with solely real data (e.g., segmentation of TS and PE in Labeled Lumbar Spine MRI), synthetic augmentation and synthetic pretraining + augmentation yielded poorer performance, while pretraining led to an improvement in performance. This suggests that synthetic augmentation may be detrimental for segmentation tasks in which real data have strong signals (e.g., strong edge correlation with masks) and synthetic data are unable to achieve similar signal strength. Pretrained weights developed based on synthetic data can boost performance in these situations by providing more ideal weight initializations that can be further refined with the strong signal from real data.

In cases of full data availability, we find that adding a moderate or full amount of synthetic data can significantly boost the performance in tasks that don’t have relatively high performance solely with real data, such as in BTCV-Abdomen, CHAOS-MRI, and CVC-ClinicDB. Future work may investigate optimal proportions for additional synthetic augmentation in different types of tasks.

Our study sought to address the significant barrier of limited medical imaging data availability for machine learning applications, which hinders model performance and limits potential medical applications. With the increased implementation of our proposed RadImageGAN synthetic paradigm, we hope to provide an additional technique for machine learning model development. This paradigm could enhance model performance on many downstream tasks in conditions of both imaging data scarcity and abundance by applying RadImageGAN-CT/MR/Gastro or developing new synthetic generators to augment relevant real datasets. Training these synthetic generators is computationally expensive, but once trained, it can be easily applied to many diverse downstream tasks. RadImageGAN-CT/MR and RadImageGAN-Gastro can already be utilized to synthetically enhance many potential downstream tasks (see **Table S1**), and we envision the future development of generators with even more diverse classes, modalities, and pathologies for research use. In addition, our study also demonstrated a scheme for developing labeled multi-class synthetic generators of both synthetic images and their respective annotation masks using BigDatasetGAN to obtain an automatically labeled dataset by manually annotating a few synthetic images. This further extends the utility of RadImageGAN for segmentation tasks. The synthetic datasets produced by RadImageGAN-Labeled can contribute to future medical imaging research as a direct method of synthetic data augmentation or an indirect method of synthetic pre-trained weight development. This scheme of RadImageGAN utility can further expand the performance of future medical imaging research.

There are also several limitations of our proposed RadImageGAN paradigm. First, to boost a specific downstream application, the generators must already contain this specific image modality and anatomy. The generators produced in this study covered limited imaging modalities, anatomies, and pathologies. For example, there are no pathologic labels from cardiac MRI images in our generators, so they are unable to enhance performance on those tasks. Secondly, imaging data such as CT and MRI are usually volumetric, but our generators were trained on individual images and are only able to generate individual image slices, as opposed to complete volumes. Third, the masks used to train RadImageGAN-Labeled were labeled by one expert, and this might lead to potential biases, thus undermining the accuracy of the resulting masks. Fourth, within one pathological label, we have a mixture of different sequences, views, anatomies, and imaging protocols, which may affect performance. For example, in the lumbar spine segmentation task, we selected the spine canal stenosis label from RadImageGAN, but this label also contains cervical spine images, which might negatively affect the performance as a data augmentation method.

In our future work, we will continue to expand the multi-class variability of RadImageGAN to generate images of more pathological labels, modalities, and anatomies. Within each pathological label, we will provide a more detailed classification of the sequences, views, and contrasts to refine the selection of imaging for synthetic enhancement. We also plan to investigate techniques to enable the generation of high-resolution volumetric imaging data and assess the value of this paradigm. Lastly, we plan to investigate the use of unsupervised learning GAN (pseudo-labeling) techniques to generate masks and further reduce the already minimal manual labeling required.

In this study, we have demonstrated the advanced capabilities of RadImageGAN to proficiently produce high-quality synthetic images from various modalities such as CT, MRI, and colonoscopy video images across an unprecedented 130 classes. Complementing this, we have

showcased the ability to apply BigDatasetGAN and automatically generate synthetic masks utilizing a weakly-supervised approach to synthetic data. The synthetic images and pre-trained weights sourced from RadImageGAN-Labeled synthetic images offer a significant enhancement to downstream segmentation applications. For data augmentation objectives, synthetic data achieves its peak performance at a 50%-100% ratio of synthetic to real data. We believe that this paradigm can be applied to many medical imaging tasks and enhance performance, particularly under low data availability conditions.

METHODS

Datasets

RadImageGAN was trained on the RadImageNet CT/MR database, a subset of the full RadImageNet database, consisting of 880,314 CT and MR images with 124 pathologic labels from 102,774 patients (10), to produce the RadImageGAN-CT/MR generator. All images were resized to 16x16, 32x32, 64x64, 128x128, 256x256, and 512x512 px resolutions for each respective model training stage. With the same training scheme, the RadImageGAN-Gastro generator was trained on a subset of the HyperKvasir dataset of colonoscopy images consisting of 6 pathological classes with sufficient samples for training (27), with a total of 5,713 images.

StyleGAN-XL

We proposed the use of StyleGAN-XL to generate high-resolution 512x512 px synthetic medical images based on our large-scale, diverse RadImageNet database and the HyperKvasir database. StyleGAN-XL is a new state-of-the-art for large-scale multi-class image synthesis that applies pre-trained feature network and classifier guidance to StyleGAN3 (36), and thus achieves better image synthesis performance on large-scale and diverse datasets (25). StyleGAN-XL is a GAN-based approach that can generate high-resolution synthetic images by using a progressive, growing approach. More synthetic layers and super-resolution layers are added to the generator as the training progresses from low resolution to high resolution. In this study, we used 8 NVIDIA DGX1-A100 GPUs for StyleGAN-XL model training. For the development of RadImageGAN, we started with low-resolution outputs at 16x16 px and progressively trained to higher-resolution outputs at 512x512 px. For the initial 16x16 stage, the stem model was trained from scratch with 10 synthetic layers and 7 head layers. The Fréchet Inception Distance (FID) was used to monitor the training process, and the model with the lowest FID score was selected as the pre-trained weights for the next higher-resolution stage. For each resolution increase, the model utilizes the previous stage's model as pre-trained weights and adds 7 additional head layers. For the final 512x512 stage, only 5 head layers were added, giving 33 head layers in total. For the 16x16 and 32x32 stages, the batch size was set to 2048, and for all higher-resolution stages, the batch size was set to 256. X-axis flip data augmentation was enabled for all stages except the final 512x512 training stage.

Downstream Datasets

Table S8 presents a summary of the four downstream datasets by modality, image series, ROI targets, and dataset size. These datasets were chosen specifically to evaluate RadImageGAN's ability to interpret unseen medical imaging data sources. A brief description of each dataset is provided below:

1. BTCV-Abdomen (28): This dataset consists of 30 randomly selected abdomen CT scans with annotations from patients undergoing a colorectal cancer chemotherapy trial or a retrospective ventral hernia study. The scans were taken in the portal venous contrast phase and captured volumes of various sizes. Each scan corresponds with a segmentation map of 13 abdominal organs. For this study, liver and kidney segmentations were used.
2. CHAOS-MRI T2 (29): This consists of 20 MRI abdominal scans with annotations from the T2-SPIR sequence. This is a subset of the full combined CT-MRI dataset. Each

dataset consists of 26 to 50 axial slices with a resolution of 256 x 256 pixels. In this study, only axial view images were utilized for evaluation. Each scan is associated with a labeled segmentation map of the kidneys, liver, and spleen. For this study, liver and kidney segmentations were used.

3. Labeled Lumbar Spine MRI (30): This dataset consists of 1,545 T2 MRI lumbar spine images obtained from an anonymized clinical study of 515 patients experiencing symptomatic back pain. Images were taken from either a sagittal or axial view and included the lowest three vertebrae and intervertebral discs (IVDs). The four ROIs were the Posterior Element (PE), Thecal Sac (TS), IVD, and the region between Anterior and Posterior (AAP) vertebrae elements. This dataset was chosen for its size and subsequent variability in age, gender, severity of illness, and imaging equipment. For this study, PE, TS, and IVD segmentations were used.
4. CVC-ClinicDB (31): The CVC-ClinicDB dataset consists of 612 still images sourced from endoscopic colonoscopy videos. Some images contain colorectal polyps. Each image corresponds to a segmentation map of the polyps.

For the BTCV-Abdomen, CHAOS-MRI, and CVC-ClinicDB datasets, all images were resized to 512x512 px. For the Labeled Lumbar Spine MRI dataset, all images were resized to 320x320 px.

Data Validation

For each downstream application, 5-fold cross-validation was conducted. In the BTCV-Abdomen and CHAOS-MRI, these two datasets were collected and resampled by patient, while the CVC-ClinicDB and Labeled Lumbar Spine MRI datasets were collected and resampled by individual image. The validation and test datasets were maintained for each fold of cross-validation.

BigDatasetGAN

We then proposed the use of BigDatasetGAN to generate high-resolution 512x512 px pixel-wise labeled synthetic medical images from RadImageGAN, turning RadImageGAN into a labeled dataset generator. BigDatasetGAN is a new state-of-the-art model extending DatasetGAN (37) that enables multi-class generation of pixel-wise annotated synthetic images from a class-conditional generative model using only a few manually annotated images per class (26). This is achieved by enhancing the pre-trained multi-class conditional generative model with a segmentation branch called a “feature interpreter” that is able to take a generator’s class-specific features and class labels as input and output a set of all pixel-wise labels for each class. We follow the methods introduced by Li et al. and use a similar feature interpreter architecture for the RadImageGAN-Labeled generator.

In this study, 50 synthetic images were manually annotated by a senior radiologist (T.D.) for each downstream task on the BTCV-Abdomen, CHAOS-MRI, and Labeled Lumbar Spine MRI. For axial CT and MRI abdomen images, liver and kidney regions were annotated. For axial MRI spine images, IVD, TS, and PE regions were annotated. For colonoscopy images, polyps were annotated. 50 synthetic colonoscopy images on the CVC-ClinicDB dataset were manually annotated for polyps by a senior machine learning applied scientist (S.H.).

During the training of RadImageGAN-Labeled, we utilized hyperparameters of 0.0001 for learning rate, 4 for batch size, and 100 training epochs.

Baseline model - nnU-Net

In this study, a 2D nnU-Net (32) was used as the baseline model for training in all segmentation tasks and data conditions since its efficiency and competency in medical segmentation tasks have been well-established and it can automatically be adapted to any given dataset. For each downstream task, each data scenario was constructed as an individual dataset for nnU-Net model development. The default training parameters were automatically generated by the *nnU-Netv2_plan_and_preprocess* function, and each model was trained with 100 epochs using the planned parameters.

Pretrained weights generated from synthetic data

For each application, five-fold cross-validation was used to train five models from scratch using a full-size dataset of synthetic images and the corresponding validation and testing datasets from each fold. The model with the best validation performance was selected as the pre-trained weights for the specific downstream dataset and associated segmentation tasks.

Statistics

For each of the downstream datasets, Shapiro-Wilk tests were conducted to evaluate the normality of each distribution of Dice scores. Since every Shapiro-Wilk test yielded a p-value less than $\alpha = 0.05$, Wilcoxon signed-rank tests were used across all pairs of columns in each downstream dataset to test for statistically significant differences in the mean Dice scores of paired observations. Both tests were performed with the Scipy package (version 1.10.1) using Python (version 3.10.9). The 95% CIs of dice scores for AI models were calculated by the bootstrap resampling with 1000 resamples.

Data Availability

In this study, the development of RadImageGAN utilized RadImageNet and HyperKvasir data. RadImageNet data is available by request via <https://www.radimagenet.com/>, and the full dataset of HyperKvasir can be downloaded via <https://osf.io/mh9sj/>. The four public segmentations datasets used in this study can be downloaded via the following links: BTCV-Abdomen (<https://www.synapse.org/#!Synapse:syn3193805/wiki/217789>), CHAOS-MRI T2 (<https://chaos.grand-challenge.org/>), Labeled Lumbar Spine MRI (<https://data.mendeley.com/datasets/zbf6b4pttk/2>), and CVC-ClinicDB (<https://www.kaggle.com/datasets/balraj98/cvcclinicdb>).

Code Availability

RadImageGAN generators and the model training process are available in the following GitHub repository: <https://github.com/lz1199704/RadImageGAN>.

Acknowledgements

X.M. was supported by the National Center for Advancing Translational Sciences (NCATS) TL1TR004420 NRSA TL1 Training Core in Transdisciplinary Clinical and Translational Science (CTSA).

Competing interests

T.D. is managing partner of RadImageNet LLC.

Author Contributions

Z.L., S.H., D.L., and X.M. developed the models and generators. Z.L. M.Y., A.Z., and X.M. created the figures. Z.L., A.Z., X.M., S.H., Z.A.F. and T.D. designed the experiments. S.H. and T.D. annotated the datasets. Z.L. and J.G. performed the statistical analysis. X.M., Z.A.F., T.D., and S.H. supervised the work. All authors wrote and reviewed the manuscript.

REFERENCES

1. Esteva A, Robicquet A, Ramsundar B, et al. A guide to deep learning in healthcare. *Nat Med*. Nature Publishing Group; 2019;25(1):24–29. doi: 10.1038/s41591-018-0316-z.
2. Sahni NR, Stein G, Zimmel R, Cutler DM. The Potential Impact of Artificial Intelligence on Healthcare Spending. *The Economics of Artificial Intelligence: Health Care Challenges*. University of Chicago Press; 2023. <https://www.nber.org/books-and-chapters/economics-artificial-intelligence-health-care-challenges/potential-impact-artificial-intelligence-healthcare-spending>. Accessed August 2, 2023.
3. LeCun Y, Bengio Y, Hinton G. Deep learning. *Nature*. Nature Publishing Group; 2015;521(7553):436–444. doi: 10.1038/nature14539.
4. Greenspan H, van Ginneken B, Summers RM. Guest Editorial Deep Learning in Medical Imaging: Overview and Future Promise of an Exciting New Technique. *IEEE Transactions on Medical Imaging*. 2016;35(5):1153–1159. doi: 10.1109/TMI.2016.2553401.
5. van Panhuis WG, Paul P, Emerson C, et al. A systematic review of barriers to data sharing in public health. *BMC Public Health*. 2014;14(1):1144. doi: 10.1186/1471-2458-14-1144.
6. Haas S, Wohlgemuth S, Echizen I, Sonehara N, Müller G. Aspects of privacy for electronic health records. *International Journal of Medical Informatics*. 2011;80(2):e26–e31. doi: 10.1016/j.ijmedinf.2010.10.001.
7. Phillips M. International data-sharing norms: from the OECD to the General Data Protection Regulation (GDPR). *Hum Genet*. 2018;137(8):575–582. doi: 10.1007/s00439-018-1919-7.
8. Na L, Yang C, Lo C-C, Zhao F, Fukuoka Y, Aswani A. Feasibility of Reidentifying Individuals in Large National Physical Activity Data Sets From Which Protected Health Information Has Been Removed With Use of Machine Learning. *JAMA Network Open*. 2018;1(8):e186040. doi: 10.1001/jamanetworkopen.2018.6040.
9. Rocher L, Hendrickx JM, de Montjoye Y-A. Estimating the success of re-identifications in incomplete datasets using generative models. *Nat Commun*. Nature Publishing Group; 2019;10(1):3069. doi: 10.1038/s41467-019-10933-3.
10. Mei X, Liu Z, Robson PM, et al. RadImageNet: An Open Radiologic Deep Learning Research Dataset for Effective Transfer Learning. *Radiology: Artificial Intelligence*. Radiological Society of North America; 2022;4(5):e210315. doi: 10.1148/ryai.210315.
11. Goodfellow IJ, Pouget-Abadie J, Mirza M, et al. Generative Adversarial Networks. *arXiv*; 2014. doi: 10.48550/arXiv.1406.2661.
12. DuMont Schütte A, Hetzel J, Gatidis S, et al. Overcoming barriers to data sharing with medical image generation: a comprehensive evaluation. *npj Digit Med*. Nature Publishing Group; 2021;4(1):1–14. doi: 10.1038/s41746-021-00507-3.
13. Shin H-C, Tenenholtz NA, Rogers JK, et al. Medical Image Synthesis for Data Augmentation and Anonymization using Generative Adversarial Networks. *arXiv*; 2018. <http://arxiv.org/abs/1807.10225>. Accessed July 25, 2023.
14. Frid-Adar M, Klang E, Amitai M, Goldberger J, Greenspan H. Synthetic data augmentation using GAN for improved liver lesion classification. 2018 IEEE 15th International Symposium on Biomedical Imaging (ISBI 2018). 2018. p. 289–293. doi: 10.1109/ISBI.2018.8363576.
15. Guo K, Chen J, Qiu T, et al. MedGAN: An adaptive GAN approach for medical image generation. *Computers in Biology and Medicine*. 2023;163:107119. doi: 10.1016/j.combiomed.2023.107119.

16. Skandarani Y, Jodoin P-M, Lalande A. GANs for Medical Image Synthesis: An Empirical Study. *Journal of Imaging*. Multidisciplinary Digital Publishing Institute; 2023;9(3):69. doi: 10.3390/jimaging9030069.
17. Gonzales A, Guruswamy G, Smith SR. Synthetic data in health care: A narrative review. *PLOS Digit Health*. 2023;2(1):e0000082. doi: 10.1371/journal.pdig.0000082.
18. Zhu J-Y, Park T, Isola P, Efros AA. Unpaired Image-to-Image Translation using Cycle-Consistent Adversarial Networks. *arXiv*; 2020. doi: 10.48550/arXiv.1703.10593.
19. Gao C, Killeen BD, Hu Y, et al. Synthetic data accelerates the development of generalizable learning-based algorithms for X-ray image analysis. *Nat Mach Intell*. Nature Publishing Group; 2023;5(3):294–308. doi: 10.1038/s42256-023-00629-1.
20. Park T, Liu M-Y, Wang T-C, Zhu J-Y. Semantic Image Synthesis with Spatially-Adaptive Normalization. *arXiv*; 2019. doi: 10.48550/arXiv.1903.07291.
21. Gheorghiu BA, Itu LM, Sharma P, et al. Improving robustness of automatic cardiac function quantification from cine magnetic resonance imaging using synthetic image data. *Sci Rep*. Nature Publishing Group; 2022;12(1):2391. doi: 10.1038/s41598-022-06315-3.
22. Jang M, Bae H, Kim M, et al. Image Turing test and its applications on synthetic chest radiographs by using the progressive growing generative adversarial network. *Sci Rep*. Nature Publishing Group; 2023;13(1):2356. doi: 10.1038/s41598-023-28175-1.
23. Mukherjee D, Saha P, Kaplun D, Sinitca A, Sarkar R. Brain tumor image generation using an aggregation of GAN models with style transfer. *Sci Rep*. Nature Publishing Group; 2022;12(1):9141. doi: 10.1038/s41598-022-12646-y.
24. Toda R, Teramoto A, Kondo M, Imaizumi K, Saito K, Fujita H. Lung cancer CT image generation from a free-form sketch using style-based pix2pix for data augmentation. *Sci Rep*. Nature Publishing Group; 2022;12(1):12867. doi: 10.1038/s41598-022-16861-5.
25. Sauer A, Schwarz K, Geiger A. StyleGAN-XL: Scaling StyleGAN to Large Diverse Datasets. *arXiv*; 2022. doi: 10.48550/arXiv.2202.00273.
26. Li D, Ling H, Kim SW, et al. BigDatasetGAN: Synthesizing ImageNet with Pixel-wise Annotations. *arXiv*; 2022. doi: 10.48550/arXiv.2201.04684.
27. Borgli H, Thambawita V, Smedsrud PH, et al. HyperKvasir, a comprehensive multi-class image and video dataset for gastrointestinal endoscopy. *Sci Data*. Nature Publishing Group; 2020;7(1):283. doi: 10.1038/s41597-020-00622-y.
28. Segmentation Outside the Cranial Vault Challenge. *Synapse*; 2015; doi: 10.7303/SYN3193805.
29. Kavur AE, Gezer NS, Barış M, et al. CHAOS Challenge - combined (CT-MR) healthy abdominal organ segmentation. *Medical Image Analysis*. 2021;69:101950. doi: 10.1016/j.media.2020.101950.
30. Sudirman S. Label Image Ground Truth Data for Lumbar Spine MRI Dataset. *Mendeley*; 2019. doi: 10.17632/ZBF6B4PTTK.2.
31. Bernal J, Sánchez FJ, Fernández-Esparrach G, Gil D, Rodríguez C, Vilariño F. WM-DOVA maps for accurate polyp highlighting in colonoscopy: Validation vs. saliency maps from physicians. *Comput Med Imaging Graph*. 2015;43:99–111. doi: 10.1016/j.compmedimag.2015.02.007.
32. Isensee F, Jaeger PF, Kohl SAA, Petersen J, Maier-Hein KH. nnU-Net: a self-configuring method for deep learning-based biomedical image segmentation. *Nat Methods*. Nature Publishing Group; 2021;18(2):203–211. doi: 10.1038/s41592-020-01008-z.
33. Radsch T, Reinke A, Weru V, et al. Labelling instructions matter in biomedical image

- analysis. *Nat Mach Intell*. Nature Publishing Group; 2023;5(3):273–283. doi: 10.1038/s42256-023-00625-5.
34. Willemink MJ, Koszek WA, Hardell C, et al. Preparing Medical Imaging Data for Machine Learning. *Radiology*. Radiological Society of North America; 2020;295(1):4–15. doi: 10.1148/radiol.2020192224.
 35. Osuala R, Skorupko G, Lazrak N, et al. medigan: a Python library of pretrained generative models for medical image synthesis. *J Med Imaging (Bellingham)*. 2023;10(6):061403. doi: 10.1117/1.JMI.10.6.061403.
 36. Karras T, Aittala M, Laine S, et al. Alias-Free Generative Adversarial Networks. arXiv; 2021. doi: 10.48550/arXiv.2106.12423.
 37. Zhang Y, Ling H, Gao J, et al. DatasetGAN: Efficient Labeled Data Factory with Minimal Human Effort. arXiv; 2021. doi: 10.48550/arXiv.2104.06490.

FIGURES

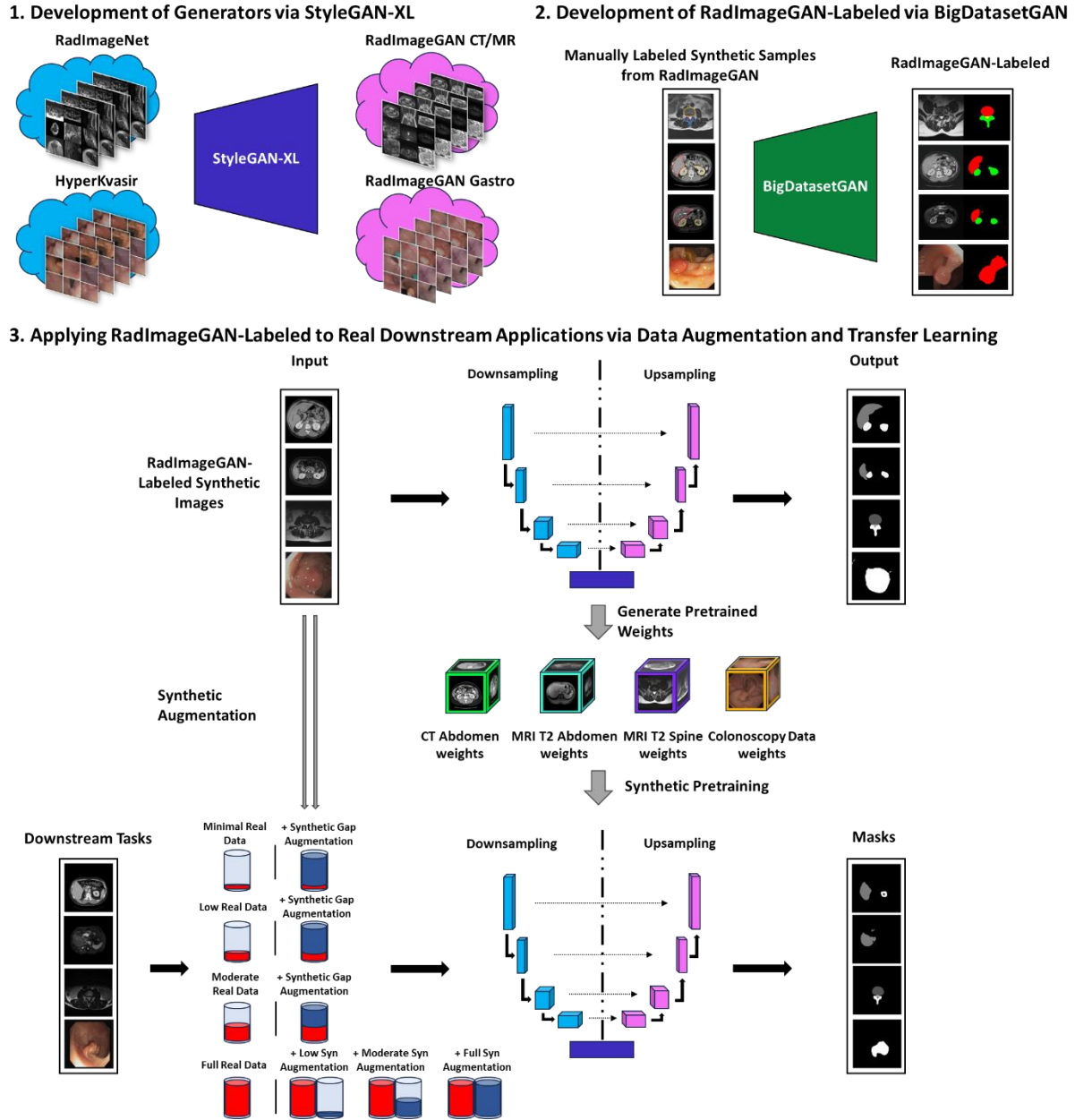


Figure 1: Overview of the study design. Step 1: RadImageGAN generators were developed by training StyleGAN-XL on a subset of the RadImageNet database and the HyperKvasir dataset of colonoscopy images; Step 2: By manually annotating 50 synthetic images for each specific downstream task, BigDatasetGAN was trained to develop RadImageGAN-Labeled for the generation of fully labeled synthetic images; Step 3: The impact of RadImageGAN-Labeled on segmentation performance is evaluated via synthetic data augmentation and/or transfer learning. Synthetic augmentation was evaluated under different data availability scenarios by taking increasingly larger subsets of the available training dataset (minimal, real, low, and full real datasets). Synthetic pretraining was evaluated using pretrained weights developed from full-size synthetic image datasets and fine-tuning on non-augmented and augmented datasets.

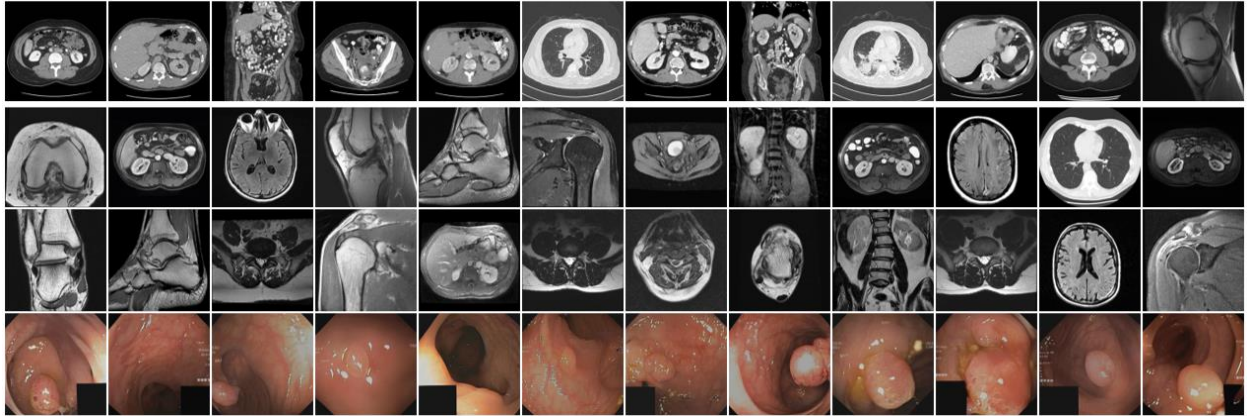


Figure 2: Representative images produced by the RadImageGAN generators across different sequences, views, and contrast.

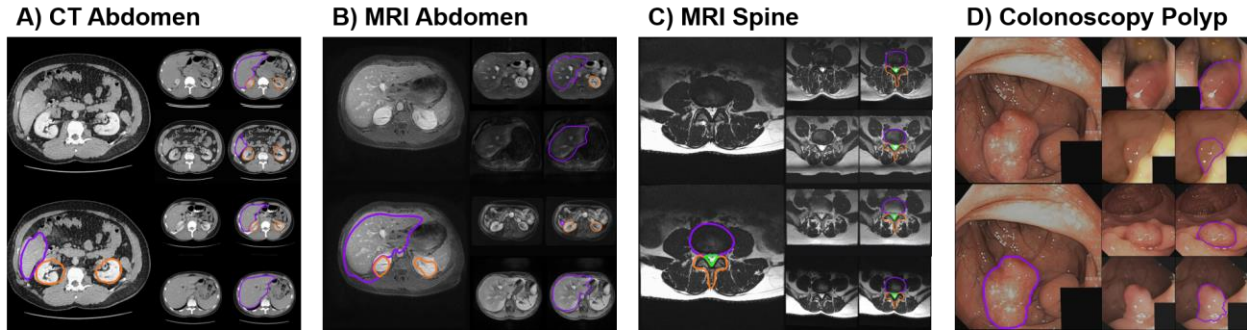


Figure 3. Representative images and masks produced by RadImageGAN-Labeled after training of BigDatasetGAN on minimal manual annotations of synthetic RadImageGAN images for each downstream dataset: A) CT Abdomen (for the BTCV-Abdomen downstream dataset; liver and kidney segmented); B) MRI Abdomen (for the CHAOS-MRI T2 downstream dataset; liver and kidney segmented); C) MRI Spine (for the Labeled Lumbar Spine MRI downstream dataset; intervertebral disc (IVD), posterior element (PE), and thecal sac (TS) segmented); D) Colonoscopy Polyps (for the CVC-ClinicDB dataset; polyps segmented).

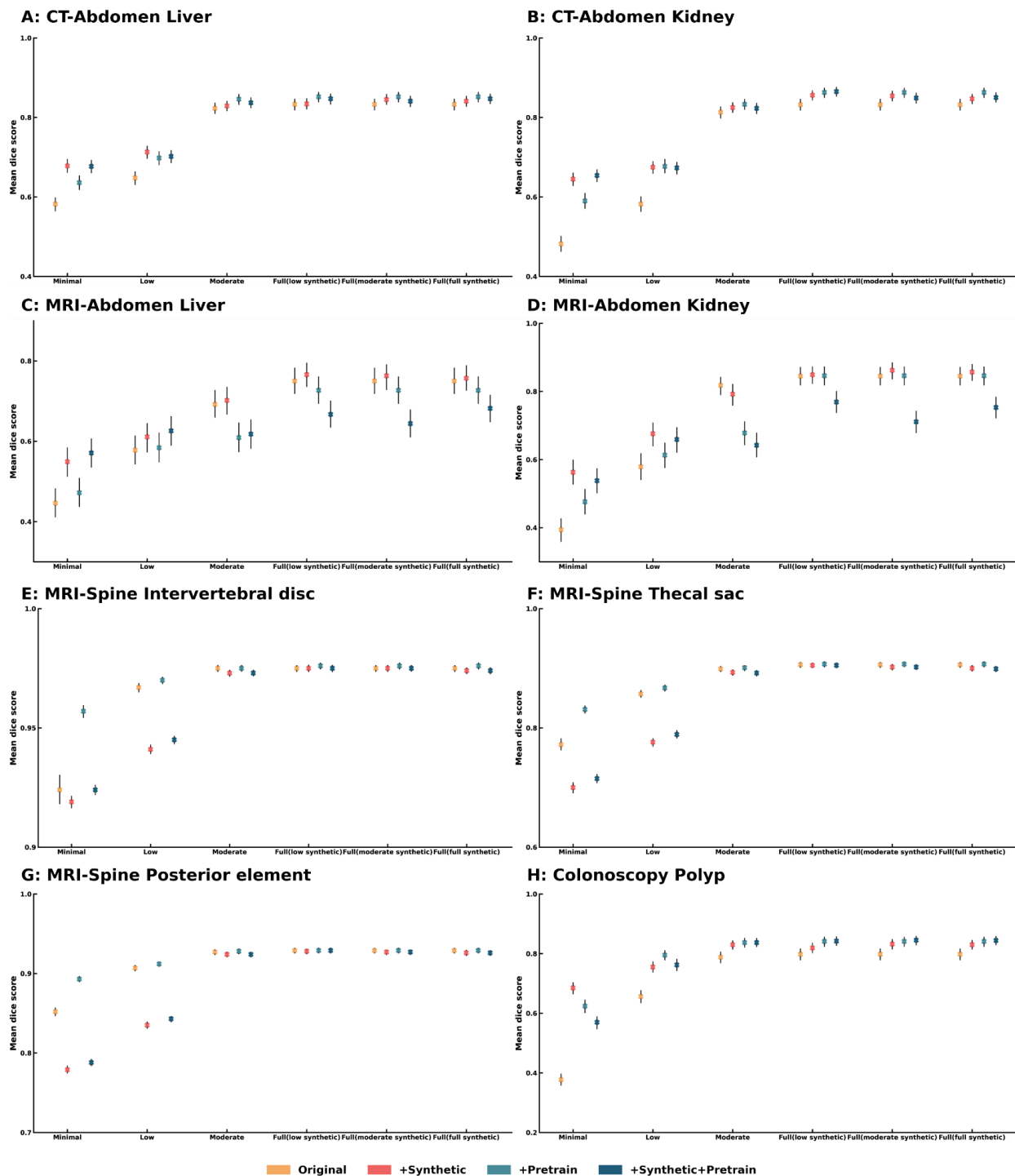


Figure 4. Bar chart comparisons of segmentation performance on downstream tasks in the four datasets without and with synthetic enhancing methods by task. Each task was grouped into 6 data conditions (minimal real data with synthetic gap augmentation, low real data with synthetic gap augmentation, moderate real data with synthetic gap augmentation, full real data with low synthetic augmentation, full real data with moderate synthetic augmentation, and full real data with full synthetic augmentation). Within each data condition, the four colors represent different

training situations of using only real data, using real data with synthetic augmentation, using real data with synthetic pretraining, and combining both synthetic methods. The black bar represents the 95% confidence interval of performance on each task: A) Liver segmentation on BTCV-Abdomen; B) Kidney segmentation on BTCV-Abdomen; C) Liver segmentation on CHAOS-MRI; D) Kidney segmentation on CHAOS-MRI; E) IVD segmentation on Labeled Lumbar Spine MRI; F) TS segmentation on Labeled Lumbar Spine MRI; G) PE segmentation on Labeled Lumbar Spine MRI; H) Polyp segmentation on CVC-ClinicDB.

TABLES

Table 1. Summary of the 10 data conditions for synthetic augmentation experiments. Various proportions of real and synthetic imaging data for training were used to simulate conditions of real data abundance or scarcity and to understand the relative effect of training with datasets enhanced with synthetic images.

Data Condition	Description	Dataset Selection Details
Minimal real data	Smallest possible imaging dataset subset for model training obtained from real patient imaging	1 scan or 1% of images from a real dataset
Minimal real data + synthetic gap augmentation	Smallest possible real imaging dataset subset augmented by a synthetic imaging dataset such that overall augmented dataset is of a similar size to the original dataset	1 scan or 1% real + 99% synthetic
Low real data	Small subset of an imaging dataset for model training obtained from real patient imaging	2 scans or 10% of images from a real dataset
Low real data + synthetic gap augmentation	Small subset of a real imaging dataset augmented by a synthetic imaging dataset such that overall augmented dataset is of a similar size to the original dataset	2 scan or 10% real + 90% synthetic
Moderate real data	~50% subset of a real imaging dataset for model training obtained from real patient imaging	50% of images/studies from a real dataset
Moderate real data + synthetic gap augmentation	~50% subset of a real imaging dataset augmented by a synthetic imaging dataset such that overall augmented dataset is of a similar size to the original dataset	50% real + 50% synthetic
Full real data	A full imaging dataset for model training obtained from real patient imaging	100% real
Full real data + low synthetic augmentation	Full real imaging dataset augmented by a synthetic imaging dataset ~10% the size of a relevant publicly available dataset	100% real +10% synthetic
Full real data + moderate synthetic augmentation	Full real imaging dataset augmented by a synthetic imaging dataset ~50% the size of a relevant publicly available dataset	100% real + 50% synthetic

Full real data + full synthetic augmentation	Full real imaging dataset augmented by a synthetic imaging dataset the same size of a relevant publicly available dataset	100% real + 100% synthetic
--	---	----------------------------

Table 2a. Performance on downstream BTCV-Abdomen segmentation tasks. Values shown are average Dice scores. 95% confidence intervals of average Dice scores are shown in parentheses.

	liver	kidney	Liver (with pretrain)	Kidney (with pretrain)
Minimal real data	0.582 (0.564, 0.600)	0.482 (0.462, 0.502)	0.636 (0.618, 0.654)	0.590 (0.570, 0.610)
Minimal real data+synthetic gap augmentation	0.678 (0.661, 0.695)	0.645 (0.628, 0.662)	0.677 (0.660, 0.694)	0.654 (0.638, 0.670)
Low real data	0.648 (0.630, 0.666)	0.582 (0.563, 0.601)	0.698 (0.680, 0.716)	0.677 (0.659, 0.695)
Low real data+synthetic gap augmentation	0.713 (0.696, 0.730)	0.675 (0.658, 0.692)	0.702 (0.685, 0.719)	0.673 (0.657, 0.689)
Moderate real data	0.823 (0.809, 0.837)	0.813 (0.798, 0.828)	0.846 (0.832, 0.860)	0.833 (0.820, 0.846)
Moderate real data+synthetic gap augmentation	0.829 (0.816, 0.842)	0.825 (0.812, 0.838)	0.837 (0.823, 0.851)	0.823 (0.809, 0.837)
Full real data	0.833 (0.818, 0.848)	0.832 (0.818, 0.846)	0.852 (0.838, 0.866)	0.863 (0.850, 0.876)
Full real data+ low synthetic augmentation	0.834 (0.820, 0.848)	0.856 (0.843, 0.869)	0.847 (0.833, 0.861)	0.865 (0.853, 0.877)
Full real data+ moderate synthetic augmentation	0.845 (0.832, 0.858)	0.854 (0.841, 0.867)	0.841 (0.826, 0.856)	0.849 (0.835, 0.863)
Full real data+ full synthetic augmentation	0.841 (0.827, 0.855)	0.847 (0.833, 0.861)	0.847 (0.834, 0.860)	0.850 (0.838, 0.862)

Table 2b. Performance on downstream CHAOS-MRI segmentation tasks. Values shown are average Dice scores. 95% confidence intervals of average Dice scores are shown in parentheses.

	liver	kidney	liver (with pretrain)	Kidney (with pretrain)
Minimal real data	0.446 (0.411, 0.481)	0.394 (0.359, 0.429)	0.472 (0.437, 0.507)	0.476 (0.439, 0.513)
Minimal real data+synthetic gap augmentation	0.549 (0.512, 0.586)	0.563 (0.527, 0.599)	0.571 (0.535, 0.607)	0.538 (0.501, 0.575)
Low real data	0.578 (0.543, 0.613)	0.579 (0.540, 0.618)	0.584 (0.548, 0.620)	0.613 (0.576, 0.650)
Low real data+synthetic gap augmentation	0.611 (0.572, 0.650)	0.676 (0.639, 0.713)	0.626 (0.589, 0.663)	0.659 (0.620, 0.698)
Moderate real data	0.692 (0.659, 0.725)	0.818 (0.789, 0.847)	0.609 (0.573, 0.645)	0.678 (0.642, 0.714)
Moderate real data+synthetic gap augmentation	0.702 (0.667, 0.737)	0.792 (0.758, 0.826)	0.618 (0.582, 0.654)	0.642 (0.607, 0.677)
Full real data	0.750 (0.718, 0.782)	0.845 (0.818, 0.872)	0.727 (0.693, 0.761)	0.846 (0.818, 0.874)
Full real data+ low synthetic augmentation	0.766 (0.735, 0.796)	0.849 (0.822, 0.876)	0.667 (0.634, 0.700)	0.769 (0.737, 0.801)
Full real data+ moderate synthetic augmentation	0.763 (0.728, 0.798)	0.862 (0.836, 0.888)	0.644 (0.610, 0.678)	0.711 (0.678, 0.744)
Full real data+ full synthetic augmentation	0.757 (0.726, 0.788)	0.857 (0.831, 0.883)	0.682 (0.648, 0.716)	0.753 (0.721, 0.785)

Table 2c. Performance on downstream Labeled Lumbar Spine MRI segmentation tasks. Values shown are average Dice scores. 95% confidence intervals of average Dice scores are shown in parentheses.

	Intervertebral Disc (IVD)	Thecal Sac (TS)	Posterior Element (PE)	IVD (with pretrain)	TS (with pretrain)	PE (with pretrain)
Minimal real data	0.924 (0.918, 0.930)	0.772 (0.762, 0.782)	0.852 (0.846, 0.858)	0.957 (0.954, 0.960)	0.831 (0.824, 0.838)	0.893 (0.889, 0.897)
Minimal real data+synthetic gap augmentation	0.919 (0.916, 0.922)	0.700 (0.690, 0.710)	0.779 (0.774, 0.784)	0.924 (0.922, 0.926)	0.715 (0.707, 0.723)	0.788 (0.784, 0.792)
Low real data	0.967 (0.965, 0.969)	0.857 (0.851, 0.863)	0.907 (0.903, 0.911)	0.970 (0.968, 0.972)	0.867 (0.861, 0.873)	0.912 (0.908, 0.916)
Low real data+synthetic gap augmentation	0.941 (0.939, 0.943)	0.776 (0.769, 0.783)	0.835 (0.831, 0.839)	0.945 (0.943, 0.947)	0.789 (0.782, 0.796)	0.843 (0.839, 0.847)
Moderate real data	0.974 (0.973, 0.977)	0.899 (0.894, 0.904)	0.927 (0.923, 0.931)	0.975 (0.974, 0.976)	0.901 (0.895, 0.907)	0.928 (0.924, 0.932)
Moderate real data+synthetic gap augmentation	0.973 (0.971, 0.975)	0.893 (0.888, 0.898)	0.924 (0.921, 0.927)	0.973 (0.972, 0.974)	0.892 (0.886, 0.898)	0.924 (0.920, 0.928)
Full real data	0.975 (0.973, 0.977)	0.906 (0.901, 0.911)	0.929 (0.925, 0.933)	0.976 (0.975, 0.977)	0.907 (0.902, 0.912)	0.929 (0.925, 0.933)
Full real data+low synthetic augmentation	0.975 (0.973, 0.977)	0.905 (0.900, 0.910)	0.928 (0.924, 0.932)	0.975 (0.973, 0.977)	0.905 (0.900, 0.910)	0.929 (0.925, 0.933)
Full real data+moderate synthetic augmentation	0.975 (0.973, 0.977)	0.902 (0.897, 0.907)	0.927 (0.923, 0.931)	0.975 (0.974, 0.976)	0.902 (0.897, 0.907)	0.927 (0.923, 0.931)
Full real data+full synthetic augmentation	0.974 (0.973, 0.975)	0.900 (0.894, 0.906)	0.926 (0.922, 0.930)	0.974 (0.973, 0.975)	0.899 (0.894, 0.904)	0.926 (0.922, 0.930)

Table 2d. Performance on downstream CVC-ClinicDB segmentation tasks. Values shown are average Dice scores. 95% confidence intervals of average Dice scores are shown in parentheses.

	polyp	Polyp (with pretrain)
Minimal real data	0.377 (0.358, 0.396)	0.624 (0.601, 0.647)
Minimal real data+synthetic gap augmentation	0.685 (0.664, 0.706)	0.697 (0.547, 0.593)
Low real data	0.656 (0.634, 0.678)	0.795 (0.778, 0.812)
Low real data+synthetic gap augmentation	0.755 (0.736, 0.774)	0.762 (0.742, 0.782)
Moderate real data	0.788 (0.768, 0.808)	0.837 (0.821, 0.853)
Moderate real data+synthetic gap augmentation	0.830 (0.814, 0.846)	0.837 (0.822, 0.852)
Full real data	0.798 (0.778, 0.818)	0.841 (0.823, 0.859)
Full real data+ low synthetic augmentation	0.819 (0.802, 0.836)	0.842 (0.826, 0.858)
Full real data+ moderate synthetic augmentation	0.832 (0.814, 0.850)	0.845 (0.828, 0.862)
Full real data+ full synthetic augmentation	0.830 (0.814, 0.846)	0.844 (0.829, 0.859)

SUPPLEMENTARY

Table S1. Summary of RadImageGAN pathological classes and imaging modalities.

Pathological Label	Class index	Imaging modality	Anatomy
abd_normal	0 (CT/MR)	CT	Abdomen
af_normal	1	MRI	ankle/foot
ankle_accessory ossicle	2	MRI	Ankle
ankle_achilles tear	3	MRI	Ankle
ankle_achilles tendinosis	4	MRI	Ankle
ankle_atfl sprain	5	MRI	Ankle
ankle_atfl tear	6	MRI	Ankle
ankle_bursitis	7	MRI	Ankle
ankle_cfl sprain	8	MRI	Ankle
ankle_cfl tear	9	MRI	Ankle
ankle_fracture	10	MRI	Ankle
ankle_ganglion	11	MRI	Ankle
ankle_joint effusion	12	MRI	Ankle
ankle_marrow edema	13	MRI	Ankle
ankle_oa	14	MRI	Ankle
ankle_osteochondral lesion	15	MRI	Ankle
ankle_pb tear	16	MRI	Ankle
ankle_pl tendinosis	17	MRI	Ankle
ankle_plantar fasciitis	18	MRI	Ankle
ankle_post op	19	MRI	Ankle
ankle_ptt tendinosis	20	MRI	Ankle
ankle_soft tissue edema	21	MRI	Ankle
ankle_tenosynovitis	22	MRI	Ankle

brain-normal	23	MRI	Brain
brain_chronic infarct	24	MRI	Brain
brain_encephalomalacia	25	MRI	Brain
brain_intra-axial metastases	26	MRI	Brain
brain_meningioma	27	MRI	Brain
brain_microvascular disease	28	MRI	Brain
foot_accessory ossicle	29	MRI	Foot
foot_achilles tendinosis	30	MRI	Foot
foot_atfl sprain	31	MRI	Foot
foot_atfl tear	32	MRI	Foot
foot_bursitis	33	MRI	Foot
foot_cfl tear	34	MRI	Foot
foot_fracture	35	MRI	Foot
foot_ganglion	36	MRI	Foot
foot_joint effusion	37	MRI	Foot
foot_marrow edema	38	MRI	Foot
foot_neuroma	39	MRI	Foot
foot_oa	40	MRI	Foot
foot_osteochondral lesion	41	MRI	Foot
foot_pb tear	42	MRI	Foot
foot_pl tendinosis	43	MRI	Foot
foot_post op	44	MRI	Foot
foot_ptt tendinosis	45	MRI	Foot
foot_soft tissue edema	46	MRI	Foot
foot_soft tissue mass	47	MRI	Foot
foot_tenosynovitis	48	MRI	Foot

hip-normal	49	MRI	Hip
hip_bursitis	50	MRI	Hip
hip_cartilage abn nos	51	MRI	Hip
hip_labral tear	52	MRI	Hip
hip_marrow edema	53	MRI	Hip
hip_osseous lesion	54	MRI	Hip
hip_post op	55	MRI	Hip
hip_soft tissue edema	56	MRI	Hip
knee-chondral abnormality	57	MRI	Knee
knee-meniscal abnormality	58	MRI	Knee
knee-normal	59	MRI	Knee
knee_acl sprain	60	MRI	Knee
knee_acl tear	61	MRI	Knee
knee_bakers cyst	62	MRI	Knee
knee_chondral wear	63	MRI	Knee
knee_effusion	64	MRI	Knee
knee_fracture	65	MRI	Knee
knee_ganglion	66	MRI	Knee
knee_iliotibial band syndrome	67	MRI	Knee
knee_loose body	68	MRI	Knee
knee_mcl sprain	69	MRI	Knee
knee_mcl tear	70	MRI	Knee
knee_meniscal degeneration	71	MRI	Knee
knee_meniscal tear	72	MRI	Knee
knee_osseous contusion	73	MRI	Knee
knee_osteoarthritis	74	MRI	Knee

knee_parameniscal cyst	75	MRI	Knee
knee_patellar tendinosis	76	MRI	Knee
knee_synovitis	77	MRI	Knee
lung-normal	78	CT	Lung
lung_abd_Bronchiectasis	79	CT	Lung
lung_abd_Emphysema	80	CT	Lung
lung_abd_Pneumonia	81	CT	Lung
lung_abd_Scar/atelectasis	82	CT	Lung
lung_abd_ascites	83	CT	Abdomen
lung_abd_diverticulitis	84	CT	Abdomen
lung_abd_diverticulosis	85	CT	Abdomen
lung_abd_gallstone	86	CT	Abdomen
lung_abd_hemangioma nos	87	CT	Abdomen
lung_abd_hepatic cyst	88	CT	Abdomen
lung_abd_hepatic lesion nos	89	CT	Abdomen
lung_abd_hiatal hernia	90	CT	Abdomen
lung_abd_hydronephrosis	91	CT	Abdomen
lung_abd_inflammation nos	92	CT	Abdomen
lung_abd_mass nos	93	CT	Abdomen
lung_abd_myoma	94	CT	Abdomen
lung_abd_ovarian/adnexal cyst	95	CT	Abdomen
lung_abd_post op	96	CT	Abdomen
lung_abd_pulm nodule	97	CT	Lung
lung_abd_renal cyst	98	CT	Abdomen
lung_abd_renal lesion nos	99	CT	Abdomen

lung_abd_sclerotic osseous lesion nos	100	CT	Abdomen
lung_abd_ureteral calculus	101	CT	Abdomen
mri_abd_hepatic cyst	102	MRI	Abdomen
mri_abd_hepatic lesion nos	103	MRI	Abdomen
mri_abd_myoma	104	MRI	Abdomen
mri_abd_ovarian/adnexal cyst	105	MRI	Abdomen
mri_abd_renal cyst	106	MRI	Abdomen
mriabd-normal	107	MRI	Abdomen
shoulder-normal	108	MRI	Shoulder
shoulder_acj oa	109	MRI	Shoulder
shoulder_biceps tendinosis	110	MRI	Shoulder
shoulder_bursitis	111	MRI	Shoulder
shoulder_capsulitis	112	MRI	Shoulder
shoulder_ghj oa	113	MRI	Shoulder
shoulder_labral tear	114	MRI	Shoulder
shoulder_post op	115	MRI	Shoulder
shoulder_supraspinatus tear	116	MRI	Shoulder
shoulder_supraspinatus tendinosis	117	MRI	Shoulder
spine-normal	118	MRI	Spine
spine_canal stenosis	119	MRI	Spine
spine_ddd	120	MRI	Spine
spine_foraminal stenosis	121	MRI	Spine
spine_herniation	122	MRI	Spine
spine_scoliosis	123	MRI	Spine

dyed_lifted_polyps	0 (Gastro)	Colonoscopy	N/A
dyed_resection_margins	1	Colonoscopy	N/A
polyps	2	Colonoscopy	N/A
pylorus	3	Colonoscopy	N/A
retroflex_stomach	4	Colonoscopy	N/A
z_line	5	Colonoscopy	N/A

Table S2. Summary of synthetic generator performance quantified by average FID and computational training time required at each training stage for RadImageGAN-CT/MR.

Output Resolution	Pretrained network	FID	Time
16x16	None	6.40	44h
32x32	16x16	7.75	53h
64x64	32x32	7.60	62h
128x128	64x64	8.85	109h
256x256	128x128	9.23	120h
512x512	256x256	9.37	183h
		Total	4,563 A100 hours

Table S3. Summary of synthetic generator performance quantified by average FID and computational training time required at each training stage for RadImageGAN-Gastro.

Output Resolution	Pretrained network	FID	Time
16x16	None	8.08	20hr
32x32	16x16	9.12	17h
64x64	32x32	11.36	16h
128x128	64x64	8.74	74h
256x256	128x128	5.50	91h
512x512	256x256	5.05	168h
		Total	3,088 V100 hours

Table S4a. P values for effects on liver segmentation performance in the BTCV-Abdomen dataset under each synthetic training method condition.

	Minimal real data	Low real data	Moderate real data	Full real data
+ Synthetic gap /full synthetic augmentation	<0.001	0.97147	<0.001	<0.001
+ pretrain	<0.001	<0.001	<0.001	<0.001
+ Synthetic gap /full Synthetic pretrain	<0.001	0.46839	<0.001	<0.001
+ low synthetic augmentation	N/A	N/A	N/A	<0.001
+ low synthetic augmentation pretrain	N/A	N/A	N/A	0.10395
+ moderate synthetic augmentation	N/A	N/A	N/A	<0.001
+ moderate synthetic augmentation pretrain	N/A	N/A	N/A	<0.001

Table S4b. P values for effects on kidney segmentation performance in the BTCV-Abdomen dataset under each synthetic training method condition.

	Minimal real data	Low real data	Moderate real data	Full real data
+ Synthetic gap /full synthetic augmentation	<0.001	<0.001	<0.001	<0.01
+ pretrain	<0.001	<0.001	<0.001	<0.001
+ Synthetic gap /full Synthetic pretrain	<0.001	<0.001	<0.001	<0.01
+ low synthetic augmentation	N/A	N/A	N/A	0.70967
+ low synthetic augmentation pretrain	N/A	N/A	N/A	0.13339
+ moderate synthetic augmentation	N/A	N/A	N/A	0.06103
+ moderate synthetic augmentation pretrain	N/A	N/A	N/A	0.3792

Table S5a. P values for effects on liver segmentation performance in the CHAOS-MRI dataset under each synthetic training method condition.

	Minimal real data	Low real data	Moderate real data	Full real data
+ Synthetic gap /full synthetic augmentation	<0.001	0.56019	0.64016	<0.05
+ pretrain	0.32463	0.11804	<0.001	<0.001
+ Full Synthetic pretrain	<0.001	0.98709	<0.001	<0.001
+ low synthetic augmentation	N/A	N/A	N/A	<0.05
+ low synthetic augmentation pretrain	N/A	N/A	N/A	<0.001
+ moderate synthetic augmentation	N/A	N/A	N/A	0.73672
+ moderate synthetic augmentation pretrain	N/A	N/A	N/A	<0.001

Table S5b. P values for effects on kidney segmentation performance in the CHAOS-MRI dataset under each synthetic training method condition.

	Minimal real data	Low real data	Moderate real data	Full real data
+ Synthetic gap /full synthetic augmentation	<0.001	<0.001	<0.01	0.36823
+ pretrain	<0.001	<0.01	<0.001	0.30913
+ Full Synthetic pretrain	<0.001	<0.001	<0.001	<0.001
+ low synthetic augmentation	N/A	N/A	N/A	0.31536
+ low synthetic augmentation pretrain	N/A	N/A	N/A	<0.001
+ moderate synthetic augmentation	N/A	N/A	N/A	0.72617
+ moderate synthetic augmentation pretrain	N/A	N/A	N/A	<0.001

Table S6a. P values for effects on IVD segmentation performance in the Labeled Lumbar Spine MRI dataset under each synthetic training method condition.

	Minimal real data	Low real data	Moderate real data	Full real data
+ Synthetic gap /full synthetic augmentation	<0.001	<0.001	<0.001	<0.001
+ pretrain	<0.001	<0.001	<0.001	<0.001
+ Full Synthetic + pretrain	<0.001	<0.001	<0.001	<0.001
+ low synthetic augmentation	N/A	N/A	N/A	<0.05
+ low synthetic augmentation + pretrain	N/A	N/A	N/A	0.11607
+ moderate synthetic augmentation	N/A	N/A	N/A	<0.001
+ moderate synthetic augmentation + pretrain	N/A	N/A	N/A	<0.001

Table S6b. P values for effects on TS segmentation performance in the Labeled Lumbar Spine MRI dataset under each synthetic training method condition.

	Minimal real data	Low real data	Moderate real data	Full real data
+ Synthetic gap /full synthetic augmentation	<0.001	<0.001	<0.001	<0.001
+ pretrain	<0.001	<0.001	<0.001	0.20726
+ Full Synthetic pretrain	<0.001	<0.001	<0.001	<0.001
+ low synthetic augmentation	N/A	N/A	N/A	<0.001
+ low synthetic augmentation pretrain	N/A	N/A	N/A	<0.01
+ moderate synthetic augmentation	N/A	N/A	N/A	<0.001
+ moderate synthetic augmentation pretrain	N/A	N/A	N/A	<0.001

Table S6c. P values for effects on PE segmentation performance in the Labeled Lumbar Spine MRI dataset under each synthetic training method condition.

	Minimal real data	Low real data	Moderate real data	Full real data
+ Synthetic gap /full synthetic augmentation	<0.001	<0.001	<0.001	<0.001
+ pretrain	<0.001	<0.001	<0.001	<0.05
+ Full Synthetic + pretrain	<0.001	<0.001	<0.001	<0.001
+ low synthetic augmentation	N/A	N/A	N/A	<0.001
+ low synthetic augmentation + pretrain	N/A	N/A	N/A	0.11752
+ moderate synthetic augmentation	N/A	N/A	N/A	<0.001
+ moderate synthetic augmentation + pretrain	N/A	N/A	N/A	<0.001

Table S7. P values for effects on polyp segmentation performance in the CVC-ClinicDB dataset under each synthetic training method condition.

	Minimal real data	Low real data	Moderate real data	Full real data
+ Synthetic gap /full synthetic augmentation	<0.001	<0.001	<0.001	<0.001
+ pretrain	<0.001	<0.001	<0.001	<0.001
+ Full Synthetic pretrain	<0.001	<0.001	<0.001	<0.001
+ low synthetic augmentation	N/A	N/A	N/A	<0.001
+ low synthetic augmentation pretrain	N/A	N/A	N/A	<0.001
+ moderate synthetic augmentation	N/A	N/A	N/A	<0.001
+ moderate synthetic augmentation pretrain	N/A	N/A	N/A	<0.001

Table S8. Downstream Task Summary

Downstream Dataset	Total training set size (scans/images)	Modality	Number of labels used in the study	RadImageGAN label
BTCV-Abdomen	30 scans	CT	2 (liver, kidney)	0 - abd_normal
CHAOS-MRI	20 scans	MRI T2	2 (liver, kidney)	107 - mri_abd_normal
Labeled Lumbar Spine MRI	1545 images	MRI T2	3 (IVD, PE, TS)	119 - spine_canal stenosis
CVC-ClinicDB	612 images	Colonoscopy	1 (polyp)	2 - Polyp